Synchronized Chaotic Mode Hopping in DBR Lasers with Delayed Opto-Electric Feedback

Yun Liu, Peter Davis, and Tahito Aida

***Abstract*—We propose and demonstrate a scheme for generating synchronized chaotic mode hopping in two wavelength-tunable lasers. Chaotic mode hopping resulting in large hops in wavelength is induced by delayed feedback of an electrical signal proportional to the intensity of the laser output which passes through an optical filter. Mode hopping among up to 11 modes was experimentally observed and optical signals in each wavelength band show a different on–off modulation time series. Analysis of the time series indicates high dimensionality. By using a unidirectional coupling method that injects part of the output of one laser into another, we can synchronize the chaotic mode hopping of two separate lasers and obtain synchronized chaotic on–off modulation patterns in multiple corresponding wavelength bands. The robustness of the synchronization with respect to the parameter mismatch and the effects of the coupling strength are investigated. The chaotic mode hopping dynamics and synchronization are well described with a numerical model that includes the characteristics of the laser tuning and the filter transmission. A multiplexed data transmission scheme using chaotic carriers is proposed and experiments demonstrate that multiple messages can be simultaneously recovered when chaos synchronization is achieved.**

***Index Terms*—Chaos, synchronization, mode hopping, optical communications, secure data transmission, spread-spectrum.**

I. Introduction

CHAOS synchronization, or synchronization of chaotic oscillators, provides a means to copy chaos, that is, to generate identical chaotic oscillations in different sites, by coupling the oscillators with suitable link signals [1], [2]. The topic of chaos synchronization has received considerable attention because of possible relevance to secure and robust communications [2], [3] and signal processing in biological systems [4], [5]. In the context of communication, an information signal containing a message is transmitted using a chaotic signal as a broad-band carrier. A key problem is the synchronization of a driven oscillator in a remote receiver by injecting a signal sent from a master oscillator in a transmitter. This is important when applying chaos to both secure communications and spectrum-spread systems where chaotic oscillations are used to mask or multiplex information in signals.

Owing to its high dimension and high bandwidth, laser chaos has been of particular interest in recent research on chaos synchronization and related secure communications using chaos [6]–[14]. Most of the laser chaos systems studied so far have been implemented using a delayed-feedback configuration due to the simplicity of implementation and feasibility of generating high dimensional dynamics [15]. In achieving synchronization of laser chaos in delayed-feedback systems, a unidirectional coupling scheme has been widely employed. Abarbanel and Kennel [16] numerically demonstrated the synchronization of two Ikeda type ring cavities via the unidirectional coupling. Recent experiments by Van Wiggeren and Roy [9] and Goedgebuer *et al.* [10] demonstrated the excellent performance of secure optical data transmission based on chaos synchronization using a particular unidirectional coupling method, i.e., the open-loop receiver scheme, which was first proposed by Volkovskii and Rulkov [17] in electronic systems.

Another attractive aspect of laser chaos is the possibility of generating signals with multiple wavelengths. This is potentially useful for communications systems using wavelength-hopping spread spectrum [18] or systems combining spread spectrum with wavelength multiplexing [19]. Chaotic variation of wavelength has been observed and studied in a number of different laser systems. Liu and Ohtsubo [20] demonstrated chaotic oscillations in a laser diode with feedback from a Twyman–Green interferometer which nonlinearly converts wavelength variation to injection current of the laser diode itself. In their experiments, attention was given to intensity variations and the accompanying wavelength oscillations were limited to a few tens of gigahertz corresponding to a subnanometer order. Recently, Larger *et al.* [21] proposed a chaotic wavelength oscillation system that consists of a wavelength-tunable laser and a birefringent plate between crossed polarizers to generate a feedback signal which is a nonlinear function of lasing wavelength. The variation range of the wavelength is extended to a few subnanometers but is still within the continuous tuning range of a single mode of the laser. They further demonstrated synchronized chaotic oscillation in two similar lasers using the unidirectional coupling scheme [10].

In our previous work [22], we reported the synchronization of chaotic mode hopping among multiple longitudinal modes in two wavelength-tunable distributed Bragg reflector (DBR) lasers. This paper extends the previous work and presents detailed discussions, both experimentally and numerically, on mode-hopping dynamics, its synchronization, and applications to secure data transmission. This paper is organized as follows. In the next section, we describe the setup of the experimental system which mainly consists of a wavelength-tunable DBR laser, an optical wavelength filter, and delayed opto-electric feedback. Characteristics of some key elements including the tuning characteristics of the light source and the optical filter transmission function are described with experimental

Manuscript received March 14, 2000; revised October 17, 2000.

The authors are with the ATR Adaptive Communications Research Laboratories, Kyoto 619-0288, Japan.

Publisher Item Identifier S 0018-9197(01)01619-0.

0018–9197/01$10.00 © 2001 IEEE

measurements. A numerical modeling of the system is briefly described at the end of this section with the details left to the Appendices. In Section III, chaotic mode hopping is investigated from two aspects: the mode switching among different modes and the optical output time series of a particular wavelength band. The key features of the mode hopping are: 1) the laser lases in one mode at a time; 2) the laser hops among different modes; and 3) the total optical power is nearly constant. The deterministic nature of the dynamics has been verified through the observation of bifurcations, dimensionality analysis, and comparison with numerical simulations. In Section IV, we show that it is possible to synchronize mode hopping between two similar lasers by coupling light output from the transmitter laser to the receiver laser. The robustness of the synchronization with respect to parameter mismatches and the effects of coupling strength are investigated with both numerical calculations and experimental measurements. In Section V, a form of multiplexed secure data transmission is demonstrated using the chaotic signals as carriers which mask the data. Based on the fact that, in the synchronized state, the modulation pattern for each wavelength band coincides with its counterpart in the receiver laser, we propose a multiplexed data encoding scheme using multiple wavelength bands. We experimentally demonstrate that two different pseudo-random sequences can be successfully recovered in the receiver side when the receiver laser is synchronized to the transmitter laser. We summarize our work in Section VI.

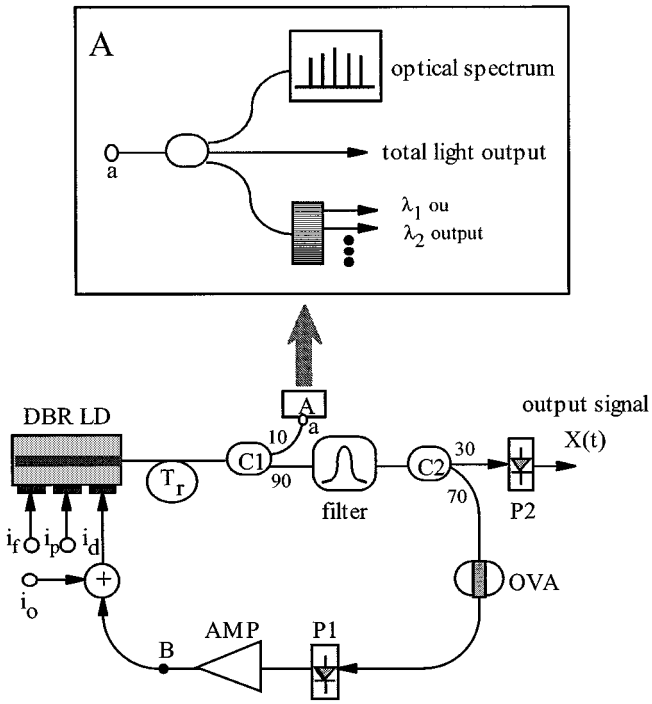

Fig. 1. Schematic diagram of experimental setup for a generation of chaotic wavelength hopping. i_d: DBR current. i_p: phase control current. i_f: LD pump injection current. i_o: offset DBR current. T_r: fiber delay line. C1, C2: fiber couplers. P1, P2: photo-receivers. OVA: optical variable attenuator. AMP: RF amplifier. Inset: spectral and intensity measurements of the laser output.

II. Experimental Setup and Modeling

A. Experimental Setup

The experimental setup is shown schematically in Fig. 1. The light source is a wavelength-tunable DBR laser diode (NEL-KELD1571) with a fiber output. An optical isolator with 55-dB isolation is employed within the laser package, which prevents external optical feedback from the fiber facet or the coupler. The wavelength of the laser can be tuned by control of the current injected into the DBR section of the laser. The light output from the DBR laser is transmitted through a fiber delay line (T_r) and then divided into two parts by a 90:10 fiber coupler C1. The first port (90%) of C1 is connected to a polarization-independent wavelength-tunable optical filter and the second port A (10%) is used for laser output monitoring as described later. The light output from the optical filter is further divided into two parts by a 70:30 fiber coupler C2. The first port (70%) of C2 is connected to a fast photo-receiver (New Focus 1611, 1 GHz bandwidth) and the detected signal is amplified with an RF amplifier (1.3 GHz bandwidth) before being fed back to drive the DBR section of the laser diode. The second port (30%) of C2 is connected to another photo-receiver (New Focus 1811, 125 MHz bandwidth) and the detected signal is monitored with a digital oscilloscope (LeCroy 9362, 750-MHz bandwidth). An optical variable attenuator (OVA) is employed in the feedback loop to adjust the feedback gain.

The light output from port A of the fiber coupler C1 is investigated in three ways, as shown in the inset of Fig. 1. First, the spectral structure of the DBR laser is measured with an optical spectrum analyzer (HP71450A, 0.1-nm resolution). Second, the intensity fluctuation of the total laser output is detected with a photo-receiver. Third, each longitudinal mode of the laser is selected using a narrow-band optical filter (0.3-nm bandwidth and center wavelength continuously tunable from 1540 to 1560 nm) and its intensity variation is measured with a photo-receiver.

The DBR laser diode used in the experiment has a structure consisting of three sections: an active section, a passive phase control (PC) section, and a passive DBR section, which are, respectively, driven by a pumping injection current i_f, a PC injection current i_p, and a DBR injection current i_d. When there is no injection in the passive sections, the laser lases at the threshold of 8 mA and in a single mode at the wavelength of about 1554 nm. The side-mode suppression ratio is more than 45 dB, which guarantees the single-mode behavior. As long as i_d and i_p are constant values, the laser is always in a single-mode state regardless of the pumping level. When i_d is increased, the laser wavelength decreases monotonically with the mode hops. The mode separation is measured to be 0.7 nm. The laser output power weakly depends on the change of i_d. Fig. 2(a) shows a measured wavelength tuning characteristic of the DBR laser. Here, i_f and i_p are fixed at 30 and 0 mA, respectively. The characteristic contains 11 segments corresponding to the 11 modes within the 7.5-nm tuning range of the laser. The variation of the PC injection current i_p, on the other hand, causes a periodic wavelength shift with the period equal to the mode separation 0.7 nm.

The 3-dB bandwidth of the commercially available optical filter (Santec OTF-310) is about 1.4 nm and the center wavelength is continuously tunable from 1540 to 1560 nm. This wide-band optical filter is used to obtain a nonlinear

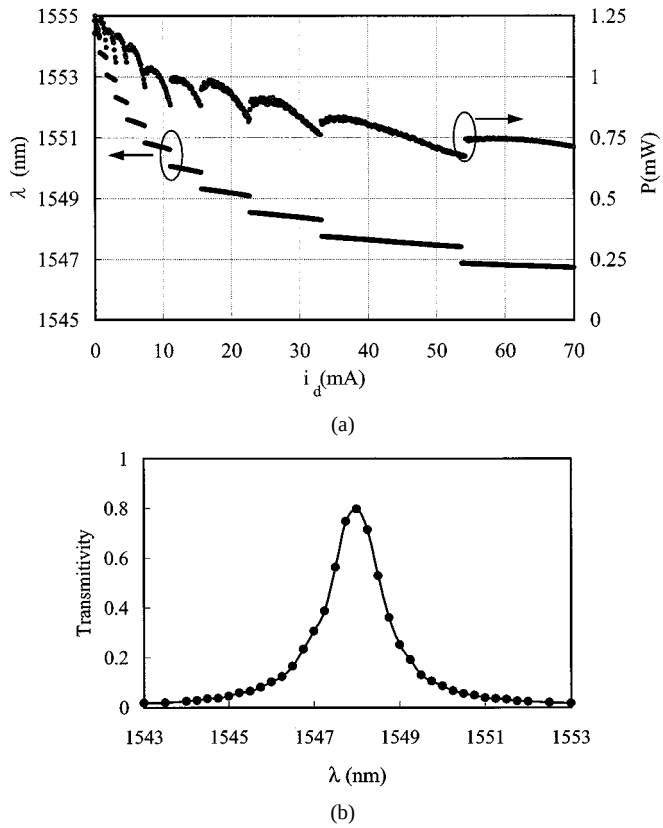

Fig. 2. Characteristics of key components of the system. (a) Wavelength tuning characteristic and accompanying power variations of the DBR laser used in the experiment at $i_f = 30$ mA and $i_p = 0$. (b) Transmission characteristic of optical filter measured at $\lambda_c = 1548$ nm.

function between the light output and the wavelength over a wide multinanometer range of wavelength variation, covering multiple longitudinal modes of the laser. Fig. 2(b) shows the measured transmission characteristic of the optical filter. The light output of the optical filter is detected with a photo-receiver and this electric signal is further amplified with an RF amplifier to generate feedback signal. Finally, the feedback signal is coupled to the DBR section of laser with a variable offset current i_o.

The response characteristics of the system are measured by opening the loop at port B in Fig. 1, driving the DBR section of the laser with an external modulation signal and measuring the output signal of the amplifier. The frequency characteristic of the open loop gain is obtained by changing the frequency of the modulation signal. The result reveals that the 3-dB cut-off frequency of the system is about 250 MHz, implying that the response time of the whole system is about 4 ns. Although both the detector and the amplifier have a bandwidth of more than 1 GHz, this frequency is mainly limited by the electrical characteristics of the laser module, namely the bandwidth of the electrical driving of the refractive index of the DBR section in the laser.

B. Numerical Modeling

The dynamics of the above system can be understood from a relatively simple dynamical model describing the relaxation of a single slow variable, such as the tuning current of the DBR section. The current injected into the DBR section determines the refractive index and, thus, the effective reflectivity of the DBR. This, in turn, determines the lasing mode, its wavelength, and amplitude [23]–[25]. Since the pumping level i_f is kept fixed, the carrier density in the active section of the laser can be regarded as constant. The relaxation of the optical field in the laser, including mode transitions, due to changes in the refractive index in the DBR section is much faster than the response of the electrical feedback driving the refractive index changes, so we consider the lasing state adiabatically follows the change of the electrical feedback signal. Therefore, we can describe the dynamics of the chaotic mode hopping in terms of the relaxation of a single slow variable such as the tuning current with delayed electrical feedback.

The dynamics of chaotic mode hopping can be mathematically modeled using a delay-differential equation for the relaxation of the tuning current with a single nonlinear feedback function representing the compounded effects of the variation of laser output wavelength and amplitude with refractive index, the optical filter transmission characteristics, and the dependence of electrical feedback signal on the optical intensity. The details of the modeling are described in the Appendices. Here, we list only the main results showing how these variables are related with each other.

In Appendix A, we show that the wavelength and output power of the DBR laser are functions of i_d, i_p, and i_f. For simplicity, we denote them as

$$\lambda(t) = f_\lambda(i_d(t); i_p, i_f) \tag{1}$$

$$P(t) = f_P(i_d(t); i_p, i_f) \tag{2}$$

where f_λ and f_p represent, respectively, variation functions of the wavelength and the power of the DBR laser. We have assumed constant values for i_p and i_f. The filter output $u(t)$ of the optical filter is described in terms of λ and P as

$$u(t) = \frac{AP(t-T_r)}{1+\frac{4}{\pi^2}F_s^2\sin^2\left[\frac{\pi(\lambda(t-T_r)-\lambda_c)}{F_s\lambda_w}\right]} \tag{3}$$

where T_r is the time delay in the loop, and $A, F_s, \lambda_c, \lambda_w$ are parameters of the filter. The deduction of the above equation and the definition of parameters are given in Appendix B. The filter output is converted to the feedback signal through the photo-receiver and the RF amplifier and, finally, the feedback signal contributes to the DBR section injection current as

$$\tau\frac{di_d(t)}{dt} + i_d(t) = i_o + \xi u(t) \tag{4}$$

where

ξ feedback gain;
τ response time of the feedback circuit;
i_o offset of the DBR injection current.

We further rewrite the equation of the mode-hopping generation system as

$$\tau\frac{di_d(t)}{dt} + i_d(t) = i_o + X(t-T_r) \tag{5}$$

$$X(t) = F[i_d(t)] = \frac{\xi A f_p(i_d(t); i_p, i_f)}{1 + \frac{4}{\pi^2} F_s^2 \sin^2\left[\frac{\pi(f_\lambda(i_d(t); i_p, i_f) - \lambda_c)}{F_s \lambda_w}\right]}. \quad (6)$$

Here, $X(t)$ is proportional to the optical filter output and is regarded as the output signal as shown in Fig. 1. We did not consider noise effects in the modeling. As shown in the following sections, the modeling agrees well with experimental results on mode hopping dynamics and its synchronization behavior despite several assumptions made.

III. Mode-Hopping Dynamics

In this section, we first describe the mode-hopping dynamics which occur when there is strong feedback with large optical bandwidth, and delay which is long compared with the response time of the wavelength tuning of the laser. For the open loop or the weak feedback condition, the DBR laser operates in a single mode with the wavelength uniquely determined by i_d and i_p and the corresponding system output X shows a constant level. When the feedback gain exceeds a certain critical level, the system output becomes unstable. There are two types of wavelength dynamics, depending on the feedback bandwidth and gain. The first type is the continuous wavelength variation of one mode, as was investigated in previous works [20], [21]. The second type is large wavelength variations with mode hops. Fig. 3 shows experimentally the measured open-loop characteristics corresponding to the above two types of wavelength dynamics. Here, $V_{\rm in}$ and $V_{\rm out}$ are, respectively, the modulation signal of the DBR injection current and the output signal of the RF amplifier in the feedback loop. When the DBR injection current is modulated within a small range, the wavelength varies within one mode and we observe a continuous nonlinear curve as shown in Fig. 3(a). On the other hand, when the wavelength variation exceeds the mode separation, mode hopping occurs and one observes a piecewise nonlinear curve as shown in Fig. 3(b). In this paper, we consider the second type of wavelength dynamics. In the following experiments, the time delay T_r introduced by the fiber line is 660 ns, and the response time τ of the system is fixed at about 4 ns.

The wavelength dynamics are investigated with two different measurements. First, the wavelength variation is converted to the light intensity variation through the optical filter and the light output of the filter is detected with a photo-receiver. The second measurement is to monitor the lasing wavelength with an optical spectrum analyzer to investigate the number of modes involved in mode hopping.

A. Bifurcation to Chaos

Bifurcation scenarios leading to the onset of chaos can be observed by varying the offset DBR current i_o, the center wavelength of the filter λ_c, or the attenuation factor of the feedback loop ξ. The oscillation waveform and bifurcation route show quite different features from the case with continuous wavelength variations [20], [21], due to the abrupt change of the lasing wavelength of the DBR laser when tuning i_d. Fig. 4 shows a period doubling bifurcation observed by varying λ_c. Other parameters are $i_o = 50$ mA, $i_p = 0$, and $i_f = 30$ mA. Fig. 4(a)

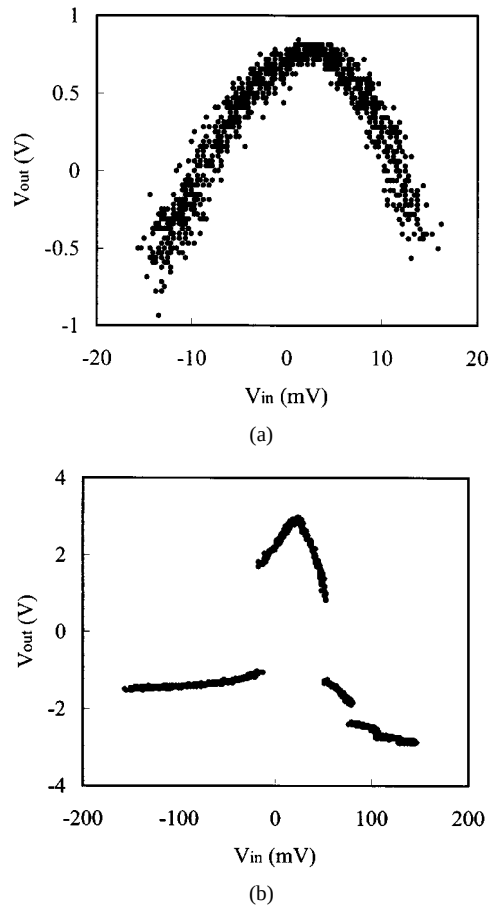

Fig. 3. Measured open-loop characteristics for different wavelength variation ranges. (a) Continuous nonlinear curve when the wavelength variation is restricted within one mode. (b) Piecewise continuous curve when the wavelength variation involves mode hops. $V_{\rm in}$: the modulation signal of DBR injection current. $V_{\rm out}$: output signal of the feedback measured at Port B in Fig. 1.

shows a period-2 waveform at $\lambda_c = 1547.5$ nm showing a periodic switch between two states with the period of about $2T_r$. Fig. 4(b) shows a period-4 waveform at $\lambda_c = 1547.0$ nm after a period-doubling bifurcation. Note that, although the period is doubled to $4T_r$, the number of intensity levels seems to be three, corresponding to three lasing modes. The onset of square wave oscillation of period $2T_r$, followed by period-doubling bifurcations and chaos, is typical of nonlinear feedback systems with long delay, such as described by delay-differential equations like (5) with a convex nonlinear feedback function and with large effective delay $T_r/\tau \gg 1$ [15]. Note that, although the signal seems almost constant over one T_r interval, in the next T_r interval it can be split into two levels. This is attributed to the discontinuous nature of the feedback as seen in the piecewise open-loop characteristic [Fig. 3(b)]. Such a splitting phenomenon shows a significant difference from previous systems [20], [21] with continuous wavelength variations. We did not observe further bifurcated periodic oscillations when λ_c is further decreased. Instead, the periodic oscillation changes to higher harmonic oscillations and the oscillation frequency increases rapidly as λ_c is reduced. At $\lambda_c = 1546.8$ nm, we observed irregular high-frequency oscillations as shown in Fig. 4(c). The time scale of (c) is different from those of (a) and (b). There is

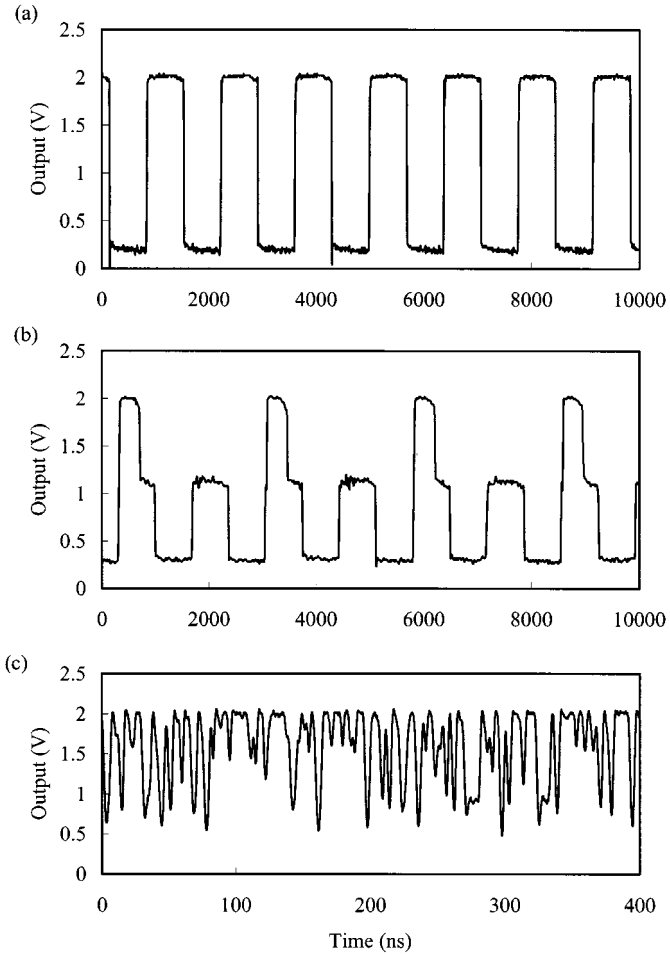

Fig. 4. Bifurcation to chaos: changes in oscillations of the output optical power with a change in the center wavelength of the optical filter. Optical power is measured at photodiode P2 in Fig. 1. (a) Period-2 waveform at $\lambda_c = 1547.5$ nm. (b) Period-4 waveform at $\lambda_c = 1547.1$ nm. (c) Chaotic waveform at $\lambda_c = 1547.0$ nm. Note that the time scale in (c) is different from that in (a) or (b). The DBR laser is operated at $i_o = 50$ mA, $i_p = 0$, and $i_f = 30$ mA.

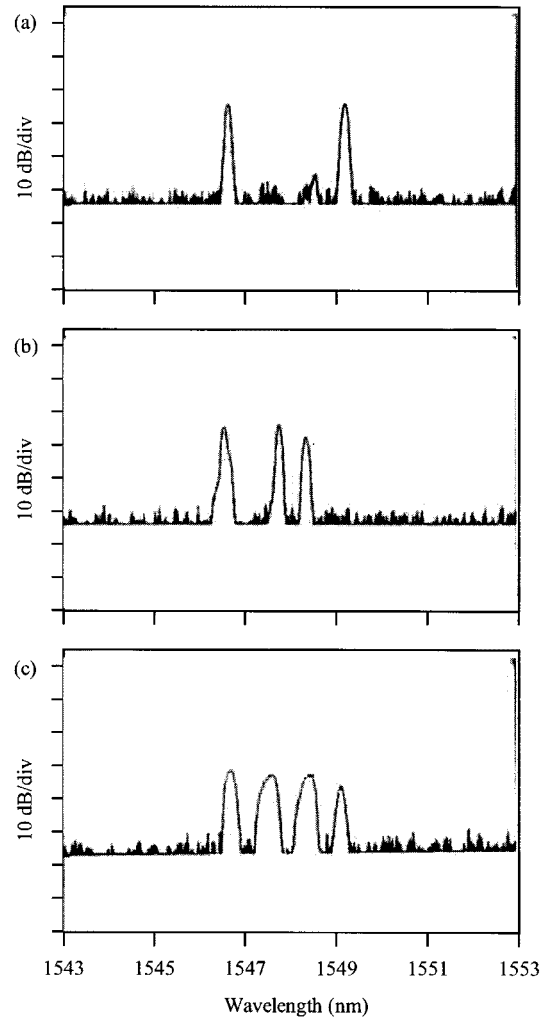

Fig. 5. Optical spectra corresponding to Fig. 4: (a) two-mode; (b) three-mode; and (c) four-mode spectrum.

a coexistence of high-frequency oscillations, i.e., for the same parameter, depending on initial conditions, different high-frequency oscillations can be excited. The coexistence of high-frequency oscillations is expected due to the large effective time delay $(T_r/\tau \gg 1)$, as described in [15].

Fig. 5 shows optical spectra corresponding to Fig. 4. Since the integration time of the optical spectrum analyzer is 20 ms, what we observed is an average within such a time interval. From this figure, one finds that the number of modes involved in the variations increased from two (period-2) to three (period-4), and finally to four (chaos).

It can be seen that different numbers of modes can be involved in chaotic dynamics depending on parameters such as the offset of the DBR injection current, the center frequency of the optical filter, and the feedback gain. Fig. 6 shows an example of an increase in the number of active modes, due to a change of the current offset from 50 mA to 20 mA. As can be seen from the tuning characteristic of Fig. 2(a), for lower offset of the tuning current, the same variation of the feedback current will result in hops over more modes. Fig. 6(a) shows an example of ten modes being active during the average time of 20 ms. Fig. 6(b) plots a portion of its corresponding time series. The corresponding RF spectrum shows a broad-band distribution. We analyzed the time series by an embedding method (using a public domain nonlinear time series analyzing software package [26]). Embedding was done for time series consisting of 120 000 experimental data points acquired at the sampling rate of 1.25 GS/s. Fig. 6(c) shows the fraction of false-nearest neighbors (FNN) versus the embedding dimension for the time series from which the series in Fig. 6(b) was taken. From Fig. 6(c), the optimal embedding dimension was estimated to be 9. Using this embedding dimension, we calculated the Lyapunov exponents to be 0.017, 0.011, 0.006, 0.002, $-0.002, -0.007, -0.014, -0.024$, and -0.057. The Lyapunov dimension was computed to be 7.6 from the above data, which indicates that the wavelength dynamics is high-dimensional chaos. The dynamics of a nonlinear system with large delay can be very complicated in general (see, for example, [15], [20], and [21]), with a complicated dependence on parameters and initial conditions, and it is not our aim in this paper to describe the dynamics in detail. Rather, here we have just presented a few examples to show that in this system we can obtain high-frequency, high-dimensional chaotic oscillations involving multiple laser modes, and that they can typi-

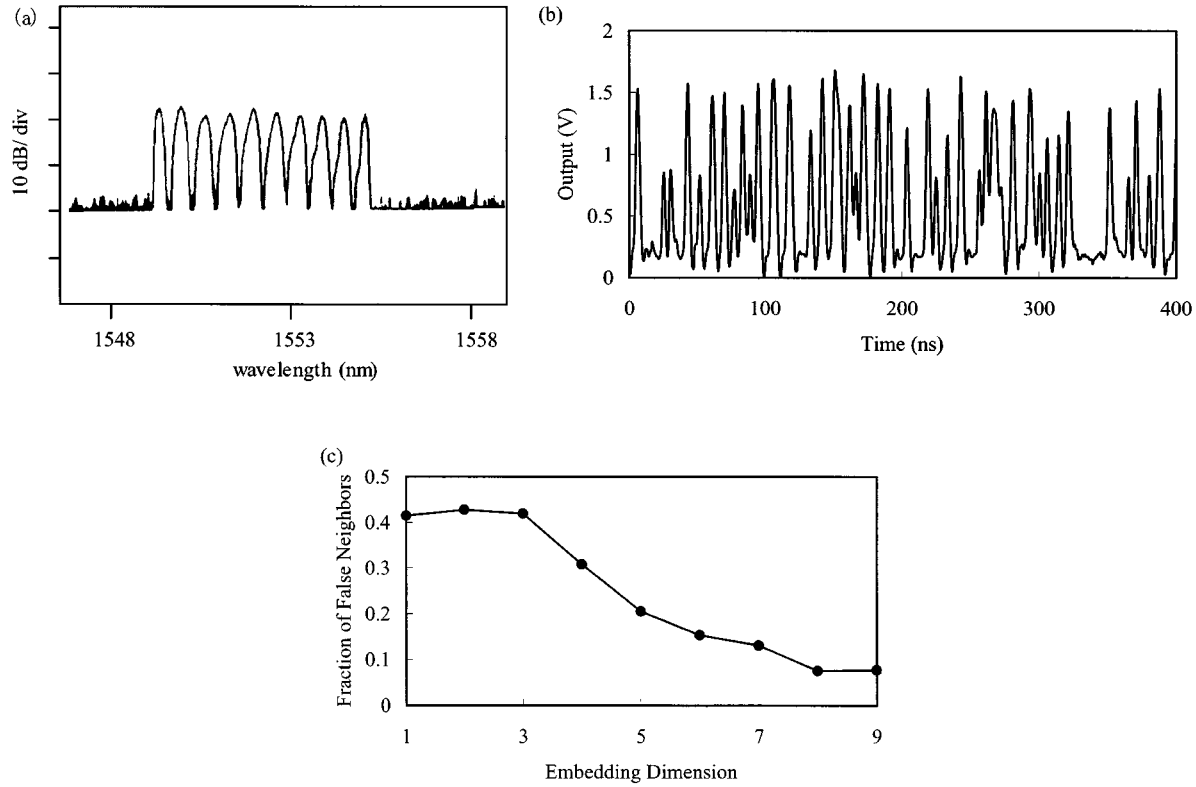

Fig. 6. Chaotic dynamics involving ten modes. Parameters are $i_o = 20$ mA, $i_p = 0$, and $i_f = 30$ mA. (a) Optical spectrum. (b) Time series of the filter output signal. (c) Faction of FNNs versus the embedding dimension using measured data.

cally appear after bifurcation from stable periodic square-wave oscillations.

B. Chaotic Mode-Hopping

Due to the long averaging time, the spectrum analyzer measurements such as in Figs. 5 and 6 show the modes which are active in the chaotic dynamics over a long time interval but they do not show how the laser hops among modes. To see how the laser hops among modes and to see the variations of individual modes, we used multiple narrow-band (bandwidth 0.3 nm) measurements of the output from the laser. Measurements were made at the position shown in inset A in the schematic of the experimental setup in Fig. 1. In Fig. 7, we present an example of observation of chaos involving three modes which shows the key features of hopping among multiple modes. With the particular oscilloscope that we used, we were able to record up to four time series simultaneously. In Fig. 7(a), the top trace shows the variation of the laser output intensity, and three other traces correspond to three different modes whose center wavelengths are 1547.6, 1548.4, and 1549.1 nm, respectively. All of these traces are plotted with the same scale. The time series show that individual modes are on–off intensity modulated with a chaotic modulation pattern. Different modes have different intensity modulation patterns and, at any specific time, most of the lasing energy is concentrated in just one of the three modes. Note that this feature of abrupt hopping in the wavelength band due to hopping among longitudinal modes of the laser is different from the behavior described in the previous works [20], [21], where there was variation of the wavelength of only a single mode. Another feature of the behavior that can be observed in Fig. 7(a) is that the total power output from the laser shows only small fluctuations during the chaotic mode hopping. This is due to the characteristic of the laser, shown in Fig. 2(a), where the output power is only weakly dependent on the lasing mode, so the laser power can stay nearly constant even if the lasing mode changes due to a large change in the tuning current.

In Fig. 7(b), we show a correlation plot of the time series of neighboring modes. The plot shows that, when intensity of one mode is high, the intensity of the other is low. This is due to the fact that the laser tends to lase in a single mode. On the other hand, it also shows that when the intensity of one mode is low it cannot be said whether the intensity of the other mode will be high or low. In this sense, the variations of the modes are not simply correlated. The example of observation of three modes shows the key features of hopping among multiple modes. Due to the limitation on the number of simultaneous traces that we could take with our oscilloscope, we were not able to make simultaneous measurements of total power and all the modes involved in the hopping for the cases of more than three modes, such as the case of four modes in Fig. 5(c), and ten modes in 6(a). However, plots like 7(b) for pairs of modes showed that the laser typically lases in just one mode at a time, regardless of the number of modes involved in the hopping. Lasing in one mode at a time is expected from the characteristics of the laser for a sufficiently slow variation of the tuning current. Multimode

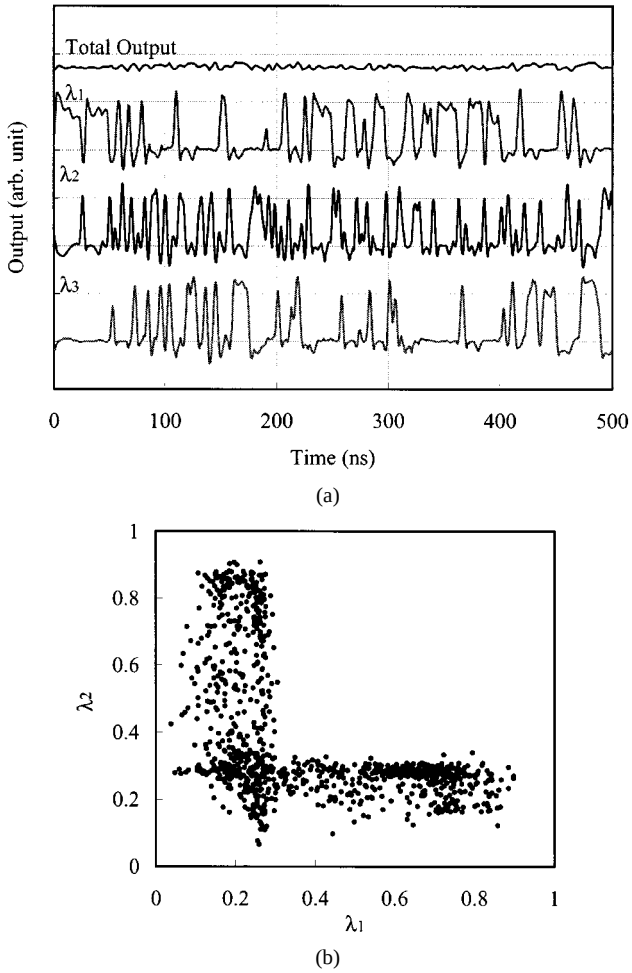

Fig. 7. Mode dynamics showing chaotic mode hopping at $i_o = 30$ mA, $i_p = 0$, and $i_f = 50$ mA, and $\lambda_c = 1549$ nm. (a) Time series of each individual mode and total laser output. (b) X–Y plot of time series between neighboring modes.

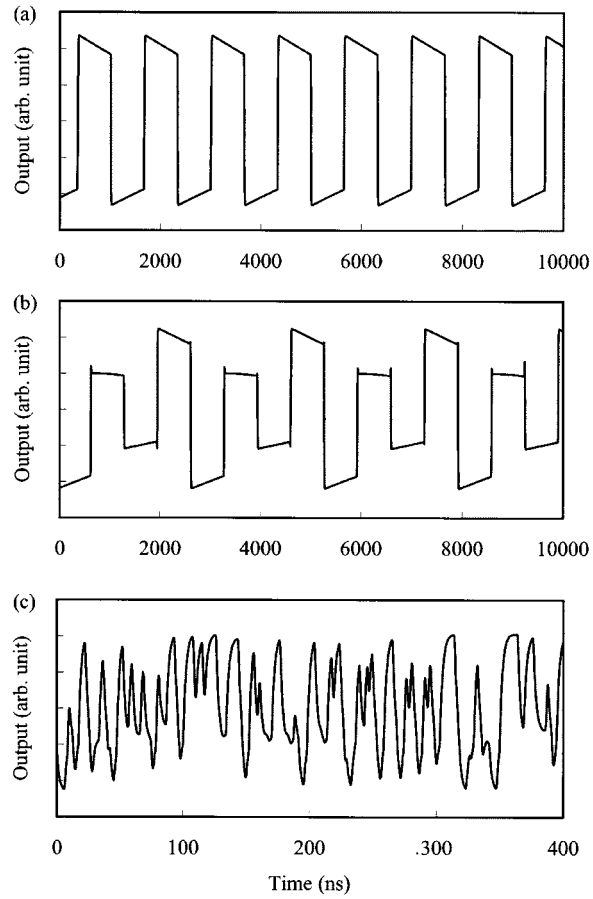

Fig. 8. Simulations of mode hopping. Parameters used are $T_r/\tau = 150$, $i_o = 50$ mA, $i_p = 0$, $\xi = 100$, and $i_f = 3.75 i_{\rm th}$ where $i_{\rm th}$ is the threshold injection current. (a) Period-2 waveform at $\lambda_c = 1547.8$ nm. (b) Period-4 waveform at $\lambda_c = 1547.5$ nm. (c) Chaotic wavelength hopping waveform at $\lambda_c = 1547.4$ nm. Note that the time scale in (c) is different from that in (a) or (b).

lasing is only expected to be a transient behavior during the hop from one mode to another.

C. Numerical Simulation of Wavelength Hopping

It is possible to reproduce the typical features of the dynamics observed in the experiment by numerical simulations using the model introduced in Section II. Here we mean to show that wavelength hopping can be obtained with a deterministic model. It is not our purpose here to reproduce the details of the dynamics. To get identical waveforms for bifurcated solutions requires very precise matching of the model functions and parameters. However, the general scenario of onset of high-frequency multimode mode-hopping chaos after bifurcation from stable period $2T_r$ square-wave oscillations is easily reproduced in the simulations. We set the value of τ to be 4 ns and that of T_r to be 600 ns. Other parameter values are either measured or determined from the modeling based on the optimum matching of DBR tuning and filter transmission characteristics between modeling results and measurements. Table I shows parameter values used in the simulations. Fig. 8 shows an example of the simulation results of the bifurcation route versus the center wavelength of the optical filter. Fig. 8(a)–(c)shows, respectively, the wavelength variations of period-2, period-4, and chaos. Here, the corresponding values of λ_c are 1547.8, 1547.5, and 1547.4 nm, respectively. Other parameters are fixed at $\xi = 100$, $i_o = 50$ mA, $i_p = 0$, and $i_f = 3.75 i_{\rm th}$ where $i_{\rm th}$ is the threshold injection current. It is found that the number of modes involved in the mode hopping increased from 2 at the period-2 state to 4 for both period-4 and chaos states. In Fig. 8(c), one observes a fast chaotic wavelength hopping time series where no periodicity could be identified. Similar to the experiments, by appropriately setting parameters, we can obtain either periodic or chaotic mode hopping among up to 11 modes in the numerical simulations. Especially, in the periodic mode-hopping state, we also observed that the signal over one T_r interval might be split into two or more levels corresponding to different longitudinal modes of the DBR laser.

We give the following remarks by summarizing experimental and numerical results.

1) Periodic or chaotic mode hopping among up to the total 11 modes of the DBR laser have been observed.
2) The output signal of the fundamental periodic mode hopping is characterized by stable period $2T_r$ square-wave oscillations.

   The number of modes involved in the fundamental period-2 mode hopping can be ≥ 2. In the latter case, the signal over one T_r interval can be split into two or more

TABLE I
PARAMETER VALUES USED IN THE NUMERICAL CALCULATIONS

Parameter	Symbol	Value	Unit
Active section of DBR LD			
Refractive index	n_{10}	3.2687	
Absorption losses	α_{10}	1125	1/m
Linear recombination time	τ_s	$2\cdot 10^{-9}$	s
Carrier density at transparency	N_0	10^{-24}	$1/m^3$
Bimolecular recombination coefficient	B_1	$8\cdot 10^{-17}$	m^3/s
Auger recombination coefficient	C_1	$7.5\cdot 10^{-41}$	m^6/s
Slope gain-carrier density	A_0	$2.5\cdot 10^{-20}$	m^2
Confinement factor	Γ_1	0.2032	
Length of active layer	L_1	300	μm
Left facet reflectivity	r_L	0.56	
Passive sections of DBR LD			
Refractive index	$n_{20}(n_{30})$	3.2144	
Absorption losses	$\alpha_{20}(\alpha_{30})$	750	1/m
Confinement factor	$\Gamma_2(\Gamma_3)$	0.3305	
Length of PC section	L_2	190	μm
Length of DBR section	L_3	480	μm
Coupling coefficient of DBR	κ	4000	1/m
Refractive index derivative with respect to carrier density	dn/dN	$-6\cdot 10^{-27}$	m^3
Absorption derivative with respect to carrier density	$d\alpha/dN$	$2.3\cdot 10^{-21}$	m^2
Bragg wavelength without current injection	λ_{B0}	1554.0	nm
Optical Wavelength Filter			
Bandwidth	λ_w	1.433	nm
Finess	F_s	31.0	
Filter transmitivity	A	0.811	

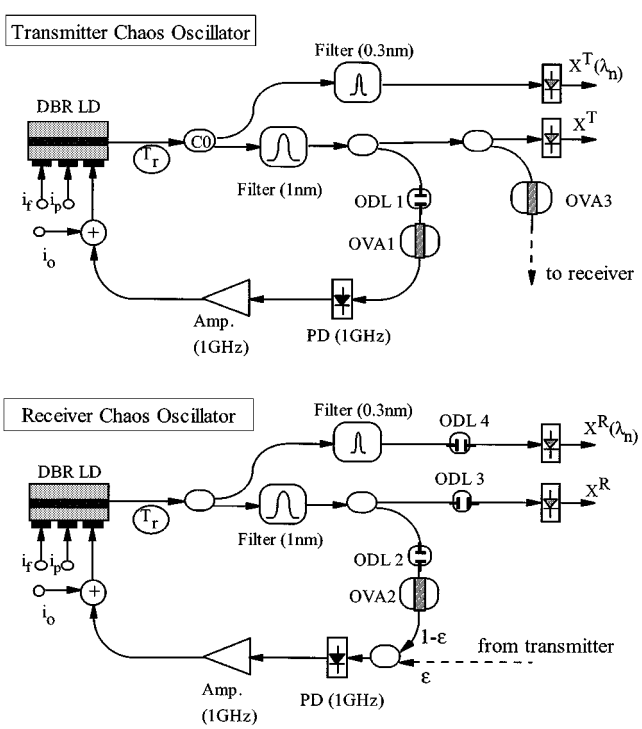

Fig. 9. Experimental setup for chaos synchronization. ODL: optical delay line. ε: coupling coefficient. Other notations are the same as in Fig. 1.

levels corresponding to different longitudinal modes of the DBR laser. Such a splitting phenomenon is due to the discontinuous nature of the nonlinear function [Fig. 3(a)].

3) Chaotic oscillations can be observed when three or more modes are involved in the mode hopping.
4) The first order of period-doubling bifurcation, period-2 to period-4, was observed. The fundamental periodic square waves coexists with high-frequency oscillations due to a large effective delay.

IV. SYNCHRONIZATION OF CHAOTIC MODE HOPPING

In this section, we show the key result of this work. We have been able to obtain synchronized chaotic mode hopping in two lasers by coupling the output of one into the other [22]. Here, we describe the synchronization of chaotic mode hopping that we achieved in two similar lasers with unidirectional coupling, in which part of the light from the transmitter laser system is coupled to the receiver laser system. The experimental setup is shown in Fig. 9. Compared with Fig. 1, a few new components are introduced in the system for synchronization. The time delay in each system is adjusted by variable optical delay lines (ODL1, ODL2) in the feedback loop. This can match delays between transmitter and receiver systems within an accuracy of 10 ps. The intensity of the synchronization signal sent from the transmitter is adjusted with an attenuator (OVA3).

A. Numerical Investigations

We start with simulations using the model introduced earlier to check the tolerance of the synchronization with respect to parameter mismatches between the transmitter and receiver sys-

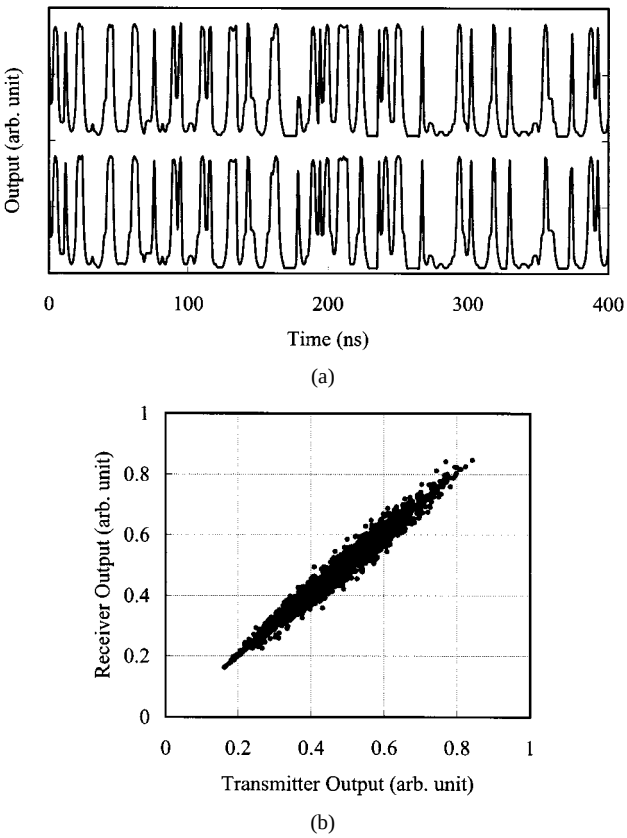

Fig. 10. Simulation of synchronization. Parameters are $T_r/\tau = 150, i_o = 20$ mA, $i_p = 0, i_f = 3.75 i_{\rm th}, \lambda_c = 1550$ nm, and $\xi = 100$. A relative parameter mismatch of 2% was assumed between the transmitter and receiver.

tems. From (5) and (6), one can rewrite the equations for the transmitter and the receiver systems shown in Fig. 9 as

$$\tau \frac{di_d^T(t)}{dt} + i_d^T(t) = X^T(t - T_r) + i_o^T \tag{7a}$$

$$X^T(t) = F\left[i_d^T(t); \lambda_c^T, \lambda_w^T, F_s^T, \xi^T\right] \tag{7b}$$

$$\tau \frac{di_d^R(t)}{dt} + i_d^R(t) = \varepsilon X^T(t - \tau_c) + (1 - \varepsilon) X^R(t - T_r) + i_o^R \tag{8a}$$

$$X^R(t) = F\left[i_d^R(t); \lambda_c^R, \lambda_w^R, F_s^R, \xi^R\right]. \tag{8b}$$

Here, we rewrite the nonlinear function $F[i_d]$ in (6) as $F[i_d; \lambda_c, \lambda_w, F_s, \xi]$ to include the effects of parameters. The superscripts T and R denote variables and parameters of the transmitter and receiver systems, respectively, and τ_c is the transmission time of the light from the transmitter to the receiver. We assumed the identical function F and values of T_r, τ, $i_p(=0)$, and i_f for both the transmitter and the receiver systems. The difference between the transmitter and the receiver systems is expressed by values of $i_o, \lambda_c, \lambda_w, F_s$, and ξ. We do not consider the effect of noise in transmission. ε denotes the coupling strength and $\varepsilon = 0$ corresponds to the noncoupled state while $\varepsilon = 1$ corresponds to the open-loop receiver system in which the feedback signal of the receiver system is completely replaced by the signal sent from the transmitter. The synchronization state corresponds to $i_d^R = i_d^T$ or $X^R = X^T$. In this experiment, we measure the difference between X^R and X^T and call this the synchronization error.

Fig. 10 shows an example of the synchronized state obtained from numerical simulations. Here, the coupling coefficient ε is set to be 1.0, which means an open-loop receiver system. The parameters i_o, λ_w, F_s, and ξ in the receiver system were assumed to be 2% larger than those in the transmitter. To make a comparison with experimental results, we take the light output intensity variations from the optical filters as the output signals and average signals over the detector bandwidth of 125 MHz. The upper and lower traces in Fig. 10(a) represent the signals of the transmitter and receiver, respectively. Fig. 10(b) shows the correlation plot between two signals. Clearly, a remarkable synchronization is achieved, even with 2% parameter mismatch. The performance of the synchronization is evaluated using a synchronization error E which is defined as

$$E = \frac{\sigma(X^T - X^R)}{\sqrt{\sigma(X^T)\sigma(X^R)}} \tag{9}$$

where σ denotes the rms average function. In Fig. 10, E is estimated to be about 2%.

B. Experimental Results of Synchronization

Before coupling the receiver with the transmitter, the parameters of the receiver system are adjusted so that the optical spectrum of the receiver laser and output waveform (amplitude, main frequency) are similar to those of the transmitter. Then, when coupling the two systems, we tune the feedback gain of the receiver system with the fiber attenuator OVA2 shown in Fig. 9 and the synchronization signal level with another attenuator OVA3 so that the total feedback strength (feedback from the receiver laser itself plus the transmitted signal from the transmitter laser) is at the same level as before coupling. The receiver output signal X^R is taken right after the optical filter and compared with the transmitter output signal X^T. Meanwhile, the light output of a particular mode in the receiver $X^R(\lambda_i)$ can also be measured with a narrow-band optical filter (0.3 nm) and compared with the corresponding signal $X^T(\lambda_i)$ in the transmitter. The time relationship between X^T and X^R or between $X^T(\lambda_i)$ and $X^R(\lambda_i)$ are adjusted with variable delay lines ODL3 and ODL4, respectively.

Fig. 11(a) shows waveforms of the transmitter and receiver system output signals in the synchronized state. The correlation plot is shown in Fig. 11(b). In Fig. 11, the synchronization error E is estimated to be 2.1%. Note that the synchronization between transmitter and receiver outputs is well recognized in Fig. 11 and the correlation distribution in Fig. 11(b) is similar to the numerical result in Fig. 10(b).

When the laser undergoes chaotic mode hopping, each mode exhibits a different modulation pattern. Here, we demonstrate that the waveforms of pairs of modes in two lasers show identical waveforms when two lasers are synchronized. We take a seven-mode case as a typical example. Fig. 12(a) shows the time-averaged optical spectrum of the laser in the chaotic mode-hopping state. In both Fig. 12(b) and (c), the top two waveforms correspond, respectively, to the total power of the light output from the transmitter and receiver systems (measured at the output of the wide-band optical filter), while the bottom

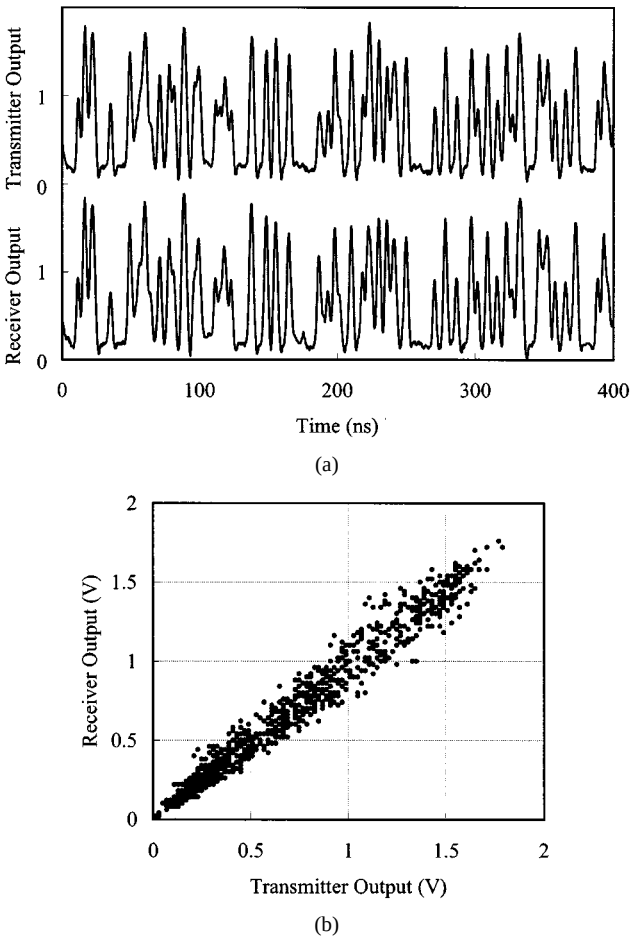

Fig. 11. Experimental observation of synchronization. (a) Waveforms of transmitter and receiver outputs. (b) Correlation plot. Parameters are $i_o = 20$ mA, $i_p = 0$, $i_f = 30$ mA, and $\lambda_c = 1550$ nm.

two show variations of the light power at one particular wavelength in the transmitter and receiver lasers (measured as shown in inset A of Fig. 1). Specifically, the bottom waveforms in Fig. 12(b) show the time series of the wavelength $\lambda = 1548.2$ nm, which corresponds to the first peak in Fig. 12(a), while those in Fig. 12(c) show the time series of $\lambda = 1550.5$ nm, the fourth peak in Fig. 12(a). In both cases, we can see excellent coincidence between transmitter and receiver outputs. Outputs for other modes were also checked and synchronization between all the corresponding modes was observed. We have also achieved chaos synchronization when mode hopping involves other mode numbers. In each case, we also observed the synchronization between modulation patterns of each specific mode pair.

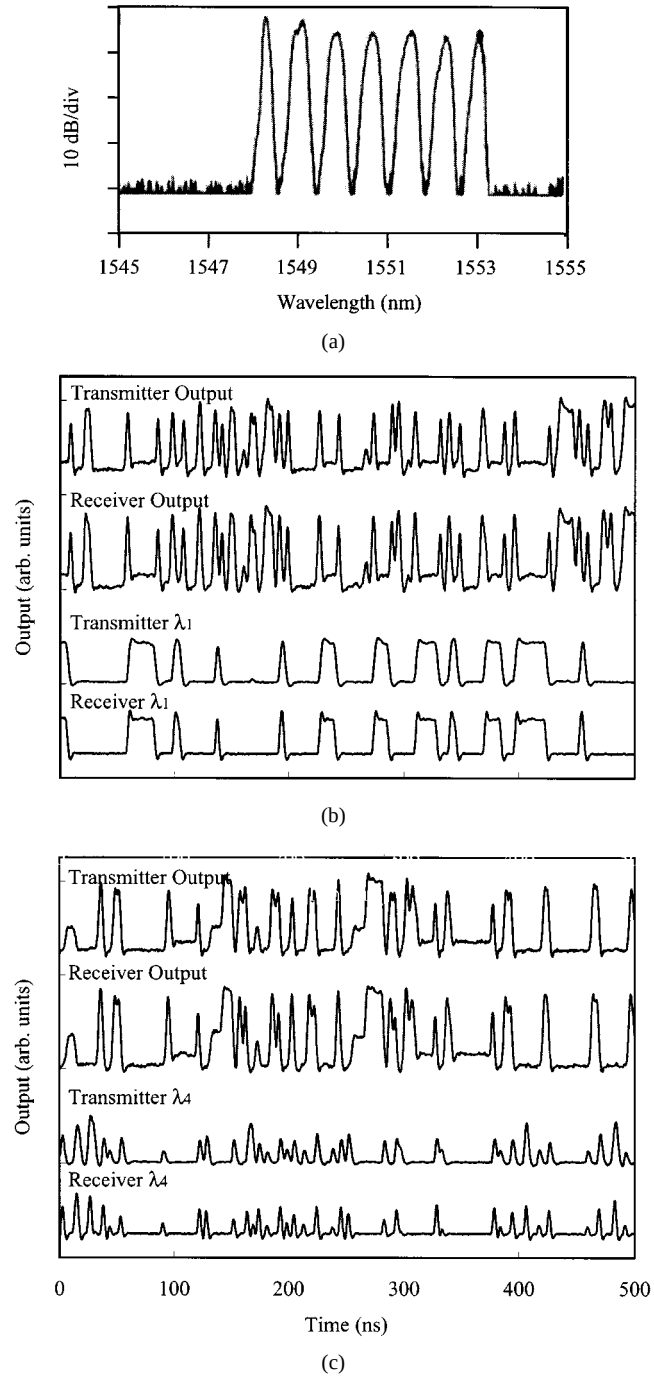

Fig. 12. Waveforms of synchronized transmitter and receiver systems at $i_o = 15$ mA, $i_p = 0$, $i_f = 30$ mA, and $\lambda_c = 1550$ nm. All traces are on the same relative scale. (a) Optical spectrum showing seven modes involved in the mode hopping. (b) Waveforms of system output and mode 1 ($\lambda = 1548.2$ nm). (c) Waveforms of system output and mode 4 ($\lambda = 1550.5$ nm).

C. Effects of Parameter Mismatch

The influence of the parameter mismatches on the synchronization was studied both numerically and experimentally. First, we numerically examined the influence of all parameters $i_o, \lambda_c, \lambda_w, F_s$, and ξ. It is found that i_o and λ_c have much stronger (usually ten times stronger) effects than the other parameters. From (7) and (8), we know that a change of i_o will linearly affect i_d and, thus, the lasing wavelength. A change in λ_c, on the other hand, results in a direct shift of the operation point and, since the mode separation of the laser is only 0.7 nm, even a subnanometer change in λ_c may result in a dramatic difference in dynamics. Fig. 13 shows the numerically calculated results of the influences of Δi_o and $\Delta\lambda_c$ on the synchronization error. Here, the coupling coefficient ε is set to be 1, i.e., an open-loop receiver is assumed. Other parameters are assumed to be identical for the transmitter and receiver systems. From Fig. 13(a), it is found that the synchronization error E varies as a linear function of Δi_o, and the slope $dE/d\Delta i_o$ is further verified to be inversely dependent on the

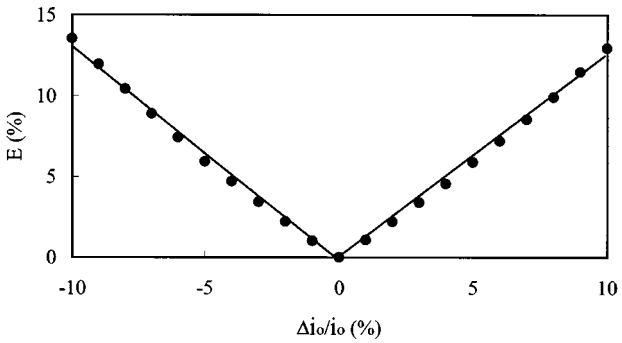

(a)

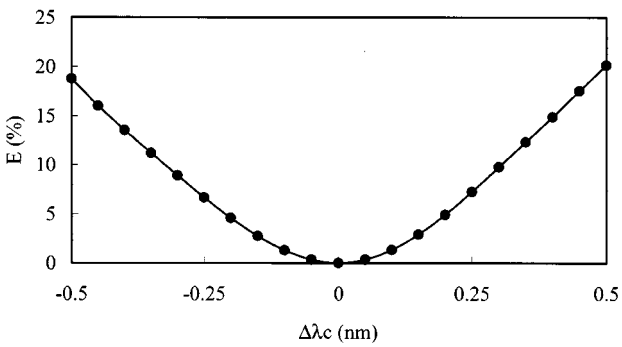

(b)

Fig. 13. Dependence of synchronization error on key parameter mismatches (simulations). Solid dots are calculated results and lines are fitted curves with $E \propto \Delta i_o$ in (a) and $E \propto \Delta\lambda_c^2$ in (b). Parameters are the same as those in Fig. 10.

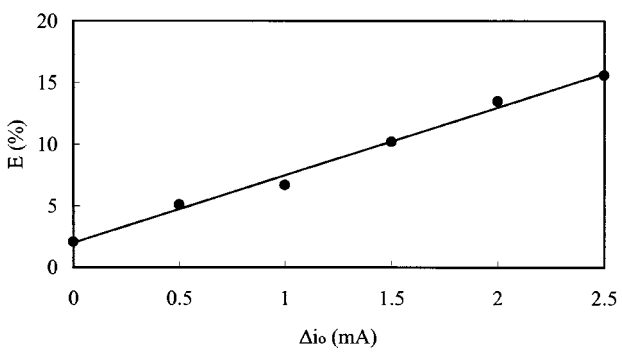

(a)

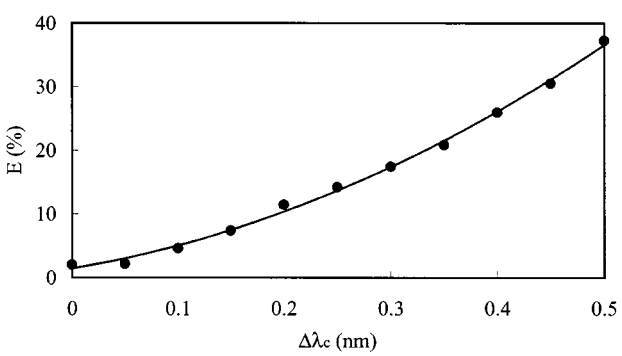

(b)

Fig. 14. Dependence of synchronization error on key parameter mismatches (experiments). Solid dots are experimentally measured results and lines are fitted curves with$E \propto \Delta i_o$ in (a) and $E \propto \Delta\lambda_c^2$ in (b). Parameters are the same as those in Fig. 11.

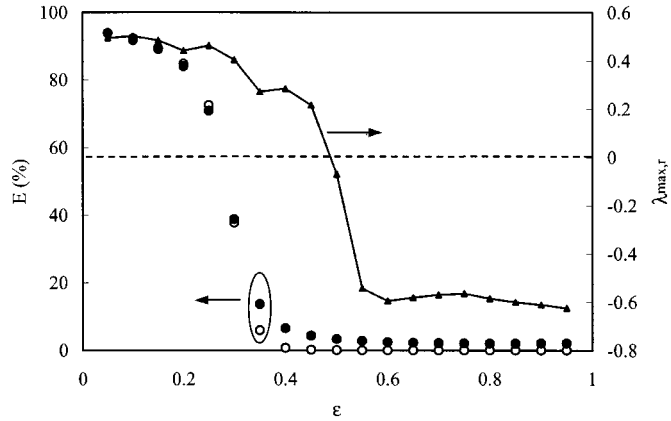

Fig. 15. Effect of coupling coefficient on synchronization error calculated from simulations. Solid line: the largest conditional Lyapunov exponent of the receiver system $\lambda_{\max,r}$. White circles: synchronization error without parameter mismatch. Black circles: synchronization error with 2% parameter mismatch. Parameters are the same as those in Fig. 10.

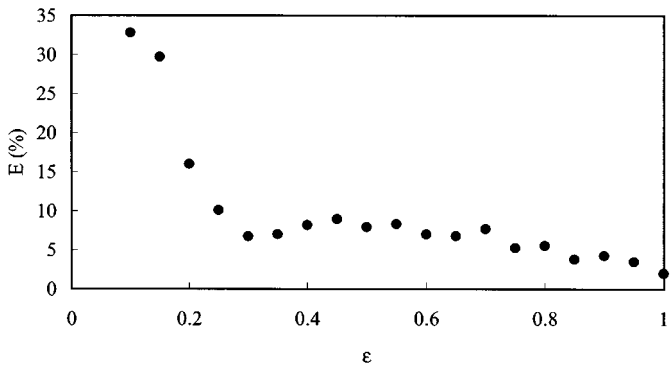

Fig. 16. Effect of coupling coefficient on synchronization error measured from experiment. ε is changed by appropriately adjusting variable attenuators OVA2 and OVA3 in Fig. 8. Parameters are the same as those in Fig. 11.

value of ε. On the other hand, when λ_c is changed, E increases as a square function of $\Delta\lambda_c$, as shown in Fig. 13(b). It is found that negative and positive parameter mismatches have almost symmetrical influences on the synchronization error.

The same parameter mismatch dependencies have also been verified in experiments. Fig. 14 shows the experimental result of the dependency of E on Δi_o [Fig. 14(a)] and $\Delta\lambda_c$ [Fig. 14(b)]. In experiments, we also observed that the negative parameter mismatch has effects on the synchronization performance similar to those of the positive mismatch. There is a pedestal of E in the experimental results due to the mismatch of other parameters and additive noise in experiment. Note that fairly good correlation between transmitter and receiver outputs can be recognized in experiments even with the synchronization error as large as 10%. We stress that the synchronization is very stable even with a few percent of parameter mismatch. Actually, under the optimal match achievable experimentally, the stable synchronization could last as long as several tens of hours!

D. Dependence on Coupling Strength

The effects of the coupling strength on the synchronization performance are important in understanding the mechanism of synchronization via unidirectional coupling. Previously, Abarbanel and Kennel [16] numerically investigated effects of the

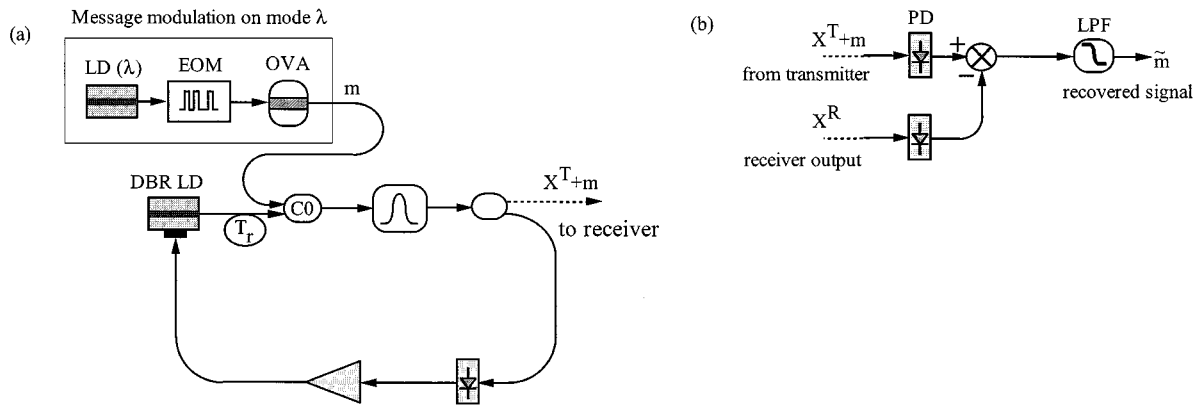

Fig. 17. Schematics of (a) message encoding and (b) decoding. EOM: electrooptic modulator. OVA: optical variable attenuator. LPF: low-pass filter. m: encoded data signal. $\bar{m}$: recovered signal.

coupling coefficient ε on the mean synchronization time in the Ikeda ring laser model. Meanwhile, experiments on synchronizations in delayed-feedback systems have concentrated on the open-loop receiver scheme [9], [10], [12], [14]. Here, we investigate the dependence of the synchronization on coupling coefficient using both numerical and experimental results. Fig. 15 shows the variation of the synchronization E versus the coupling coefficient ε obtained from the numerical simulations. In order to make a suitable comparison with experiments, we calculated two sets of E. White circles represent E calculated without parameter mismatch and black dots represent E calculated with the assumption that parameters i_o, λ_w, F_s, and ξ in the receiver are 2% larger than those in transmitter. We also calculated the largest conditional Lyapunov exponent [2], [16] of the receiver system $\lambda_{\max,r}$ for reference. The polarity of $\lambda_{\max,r}$ reflects the stability of the receiver chaotic oscillator when no signal is sent from the transmitter. Both E and $\lambda_{\max,r}$ are computed over an ensemble of initial conditions. Two significant conclusions are drawn from Fig. 15.

1) When there is no parameter mismatch, E converges to zero in the region of negative $\lambda_{\max,r}$, i.e., a complete locking of the receiver chaotic oscillator to the transmitter chaotic oscillator occurs in the parameter region of negative $\lambda_{\max,r}$.
2) When there exists a parameter mismatch, E changes little in the region $\lambda_{\max,r} < 0$ but shows a drastic increase near the boundary $\lambda_{\max,r} = 0$ and shoots up to several tens of percent after $\lambda_{\max,r} > 0$.

We further verify the dependence of the synchronization performance on the coupling strength in experiments. To vary the coupling coefficient, we need to adjust attenuators OVA2 and OVA3 accordingly to keep the constant oscillation magnitude of the receiver output. Fig. 16 shows the synchronization error as a function of ε measured in experiments. Although details in Fig. 16 and Fig. 15 require further studies, it can be recognized that the two results (Fig. 16 and black dots in Fig. 15) are consistent regarding the variation of E versus ε, i.e., E does not show much change for large values of ε but exhibits a dramatic and abrupt increase when ε becomes smaller than a critical value, indicating the collapse of synchronization.

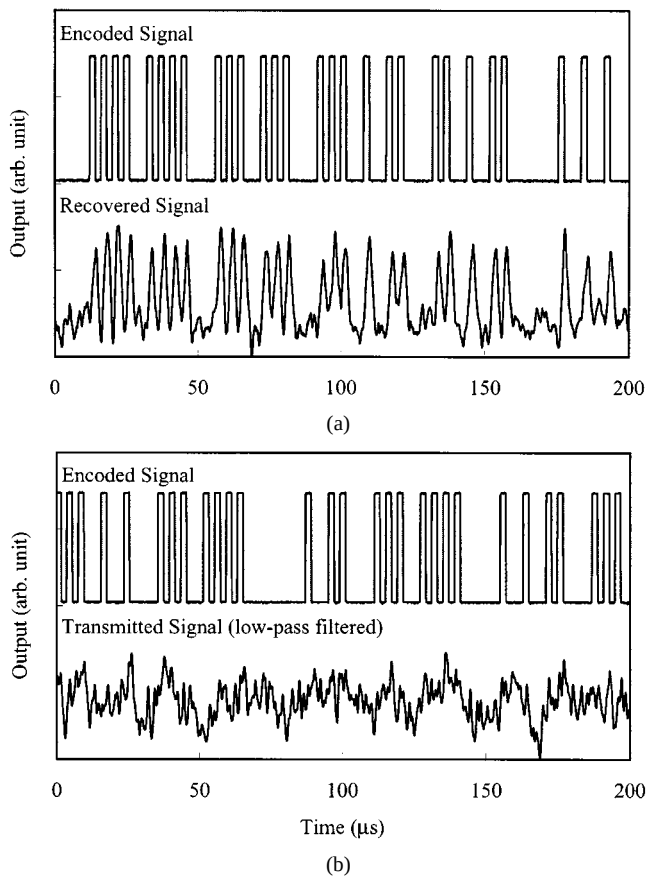

Fig. 18. Experimental results of message transmission and recovery based on chaos synchronization. (a) Upper trace: a portion of RZ pseudo-random sequence encoded at the transmitter. Lower trace: signal recovered at the receiver using the synchronized signal. (b) Upper trace: encoded pseudo-random sequence. Lower trace: signal recovered by directly integrating the transmitted signal.

V. Data Transmission with Chaos Synchronization

As an example of an application of chaos synchronization, we demonstrate data transmission using chaotic signals as masking carriers. An optical data signal is produced by modulating a light source with a pseudo-random sequence m. The optical data signal was injected into the coupler C0 as shown in Fig. 17(a). In the receiver system, the chaotic signal is recovered based on the

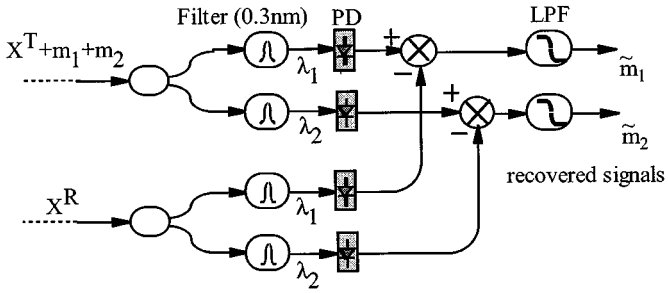

Fig. 19. Schematic of message decoding circuit in the receiver system for two-wavelength data transmission. m_1, m_2: data signals encoded on λ_1 and λ_2, respectively. $\bar{m}_1$, $\bar{m}_2$: recovered signals of m_1 and m_2.

synchronization between two lasers. By subtracting the recovered signal from the transmitted signal, we get an error signal that, for perfect synchronization, is proportional to the encoded message. In the presence of imperfect synchronization due to parameter mismatch and noise, the encoded message can be recovered after an appropriate integration of the error signal, as shown in Fig. 17(b). The minimum relative intensity of the injected optical data signal depends on both the synchronization error and the integration time. In our experimental scheme, we found that a data signal with relative intensity of 1% could be successfully masked and recovered at a bit rate of 1 Mbit/s.

Fig. 18 shows an example of message transmission and recovery in the experiment at a bit rate of 0.5 Mbits/s. In Fig. 18(a), the upper trace shows a portion of the return-to-zero (RZ) pseudo-random sequence encoded at the transmitter system, and the lower trace shows the signal recovered at the receiver system. It can be recognized that the peak positions of the recovered signal coincide well with the encoded pulses. We verified the effectiveness of the masking of the data signal by directly filtering the transmitted signal $(X^T + m)$ to show that the message cannot be simply obtained from the transmitted signal alone. A result is shown in Fig. 18(b). Here, the upper trace shows another RZ data sequence, and the lower trace shows the result of direct integration of the transmitted signal. There is no noticeable correspondence between the two signals. This demonstrates that the encoded message can only be recovered using the synchronized chaotic carrier signal X^R regenerated in the receiver system.

Since each mode has a different on–off modulation pattern, it is also possible to use each wavelength as a separate carrier and encode a different message on each carrier. We demonstrate such data multiplexing in our setup. To this end, we inject different pseudo-random data sequences at different wavelengths at the transmitter side. The wavelength of the injection light is chosen to match that of the assigned mode in the mode-hopping laser. At the receiver side, for each data carrier wavelength, we simultaneously filter out the transmitted signal and the receiver outputs with a pair of narrow band filters set at the same center wavelength. Multiple error signals can be extracted by subtracting the corresponding pairs of the detected signals. In this way, one can simultaneously mask multiple messages using a single mode-hopping laser.

Fig. 19 shows a schematic showing how to simultaneously recover two messages encoded in two different wavelength bands.

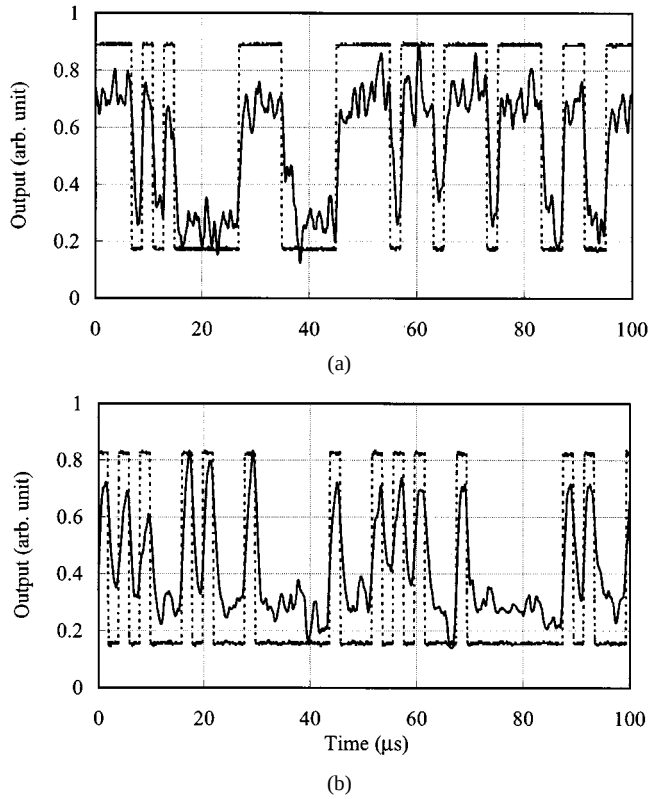

Fig. 20. Experimental result of multiplexed data transmission based on synchronization of seven-mode chaotic mode hopping (Fig. 11). (a) Dashed line: a portion of NRZ pseudo-random sequence encoded on wavelength $\lambda_1 = 1550.5$ nm. Solid line: corresponding recovered signal at the receiver. (b) Dashed line: a portion of RZ pseudo-random sequence encoded on wavelength $\lambda_2 = 1551.2$ nm. Solid line: corresponding recovered signal at the receiver.

An example of two-channel secure data transmission based on the synchronization of seven-mode hopping (Fig. 12) is shown in Fig. 20. Two wavelengths $\lambda_1 = 1550.5$ nm and $\lambda_2 = 1551.2$ nm, which correspond to the fourth and fifth peaks in Fig. 12(a), respectively, are used to encode two different messages. In this experiment, we simultaneously encode a NRZ pseudo-random sequence m_1 on λ_1 and a RZ pseudo-random sequence m_2 on λ_2. Both sequences have the same bit rate of 0.5 Mbits/s. Fig. 20(a) shows the data recovery on λ_1 and Fig. 20(b) shows that on λ_2. In each figure, the dashed line shows a portion of the pseudo-random sequence encoded at the transmitter while the solid line shows the corresponding recovered signal at the receiver. We find both messages are well recovered. It is noted that adding the second message does not degrade the recovery of the first one compared with the single message case. This experimental scheme can be expanded to multiplex messages on more wavelength bands.

VI. Conclusion

We have demonstrated a scheme in which chaotic mode hopping can be generated, synchronized and used for multiplexed data transmission. The chaotic mode hopping among multiple longitudinal modes of a laser can be generated in a delayed feedback system which consists of a wavelength tunable DBR laser and an optical filter. When chaotic mode hopping occurs,

each mode exhibits a different on–off intensity oscillation pattern while the total laser output intensity shows a nearly constant level. The chaotic nature of the mode-hopping dynamics was characterized by the observation of bifurcation from periodic oscillations and dimensionality analysis. Numerical simulation of a deterministic model showed similar bifurcation to chaotic mode hopping, and accordingly verified the underlying determinism in the observed phenomenon.

Synchronization of mode hopping between the transmitter and receiver lasers has been achieved by a unidirectional coupling of part of the light output from the transmitter laser to the receiver laser. Synchronization was observed between the on–off intensity modulation patterns of each pair of corresponding longitudinal laser modes. Evaluations on synchronization performance have been performed and the results indicate the synchronization can be achieved for a large parameter range and with a very good robustness.

Synchronization of chaotic mode-hopping stimulates us to consider the possibilities of secure communication or spectrum spreading applications using chaotic signals. In this paper, we have proposed a multiplexed secure data transmission scheme using the simultaneous synchronization of multiple time-varying signals at different wavelengths. A preliminary experiment on two-channel data transmission and decoding has been successfully demonstrated. It is noted that the limitations on the number of modes, the mode separation, and the hopping speed in the synchronized chaotic wavelength hopping scheme proposed in this paper are only due to the specifications of the laser devices and can be improved with the development of components. Considering its simple implementation and excellent synchronization robustness, this synchronized chaotic wavelength hopping scheme is very promising for applications to data transmission using chaos.

Appendix A
Modeling of Tuning Characteristic of the DBR Laser Diode

The lasing condition of a DBR laser diode with three sections is written as [23]

$$r_L \cdot r_{\mathrm{DBR}} \exp[-j(2k_1L_1 + 2k_2L_2)] = 1 \tag{A1}$$

where r_{DBR} is the effective reflectivity of the DBR section including the reflectivity at the right facet and r_L is the facet reflectivity at the left end of the laser. The complex wavenumbers for the three sections are given by

$$k_1(\omega, N_1) = \frac{\omega}{c} n_1(\omega, N_1) + j\alpha_{\mathrm{th}} \tag{A2}$$

$$k_i(\omega, N_i) = \frac{\omega}{c} n_i(\omega, N_i) - j\alpha_i(\omega, N_i), \quad i = 2 \text{ or } 3 \tag{A3}$$

where $\alpha_{\mathrm{th}} = g - \alpha_1$ is the net gain in the active section with g being the material gain and α_1 the internal absorption. α_i are the waveguide absorptions of the passive sections. r_{DBR} can be explicitly expressed as [24], [25]

$$r_{\mathrm{DBR}} = \frac{-j\kappa \sinh(\gamma L_3)}{\gamma \cosh(\gamma L_3) + (\alpha_3 + j\Delta\beta)\sinh(\gamma L_3)} \tag{A4}$$

with $\gamma = \sqrt{\kappa^2 + (\alpha_3 + j\Delta\beta)^2}$ and $\Delta\beta = 2\pi n_3/\lambda - 2\pi n_{30}/\lambda_B$ where κ is the coupling coefficient of the DBR structure, n_{30} is the refractive index in DBR section without injection, and λ_B denotes the Bragg wavelength.

Usually, the dynamics of the laser diode is described by a group of rate equations involving the optical power, phase, and carrier density in the active region. Since the pumping level is kept fixed, the carrier density in the active section of the laser can be regarded as constant. Furthermore, the relaxation of the optical field in the laser, including the mode transition due to changes of the refractive index in the DBR section, are assumed to be fast enough compared to the response of the electrical feedback driving the refractive index changes, so we can assume the lasing state adiabatically follows the change of the electrical feedback signal. Therefore, we only consider the stationary state in the rate equation. The stationary states of the threshold carrier density N_{th}, the injection current density J_{th}, and the output power of the laser P are given by the following three equations, respectively [27]:

$$N_{\mathrm{th}} = N_0 + \frac{2(\alpha_{\mathrm{th}} + \alpha_1)}{A_0\Gamma_1} \tag{A5}$$

$$J_{\mathrm{th}}/eV_1 = N_{\mathrm{th}}\left(1/\tau_s + B_1N_{\mathrm{th}} + C_1N_{\mathrm{th}}^2\right) \tag{A6}$$

$$P = \eta \frac{J_b - J_{\mathrm{th}}}{v_g A_0 (N_{\mathrm{th}} - N_0)} \tag{A7}$$

where

- τ_s linear recombination time;
- B_1 bimolecular recombination coefficient;
- C_1 Auger recombination coefficient;
- Γ_1 confinement factor in the active region;
- V_1 volume of the active section;
- v_g group velocity of light;
- A_0 slope of gain-carrier density relation;
- N_0 carrier density at the point of zero gain;
- P emitted light power calculated from the uniform photon density along the active section.

The dependencies of the lasing condition on i_d and i_p can be treated in similar way and here we only describe the effect of i_d. When i_d is changed, the carrier density is changed according to

$$N_{\mathrm{DBR}} = \left(\frac{i_d}{eV_3C_3}\right)^{\frac{1}{3}} \tag{A8}$$

where

- e electron charge;
- V_3 volume of the DBR section;
- C_3 corresponding Auger recombination coefficient.

We have made the assumption that the total rate of spontaneous recombination per unit volume is due to nonradiative Auger processes. The change of the carrier density results in changes of the refractive index, the loss, and the Bragg wavelength of the DBR structure like [23]

$$n_3 = n_{30} + \Gamma_3(dn/dN)N_{\mathrm{DBR}} \tag{A9}$$

$$\alpha_3 = \alpha_{30} + \Gamma_3(d\alpha/dN)N_{\mathrm{DBR}} \tag{A10}$$

$$\lambda_B = \frac{\lambda_{B0}}{1 - \Gamma_3(N_{\mathrm{DBR}}/n_{30})(dn/dN)} \tag{A11}$$

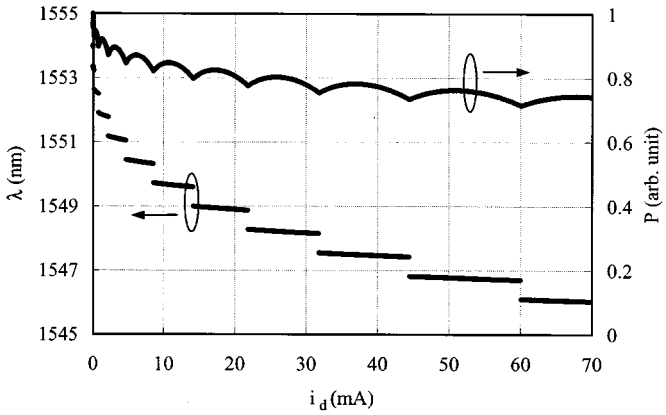

Fig. 21. Calculated result of tuning characteristics of DBR laser diode based on the numerical model. $i_p = 0$ and $i_f = 3.75 i_{\rm th}$ where $i_{\rm th}$ is the threshold injection current, other parameter values are listed in Table I.

where Γ_3 is the confinement factor in the DBR region, and n_{30} and α_{30} are, respectively, the refractive index and absorption factor at $i_d = 0$. The calculations are performed as follows. When the DBR injection current is changed, we first calculate variations of the refractive index, the absorption, and the Bragg wavelength according to (A8)–(A11). Next we calculate the DBR reflectivity from (A4) and obtain multiple modes from (A1) using $r_{\rm DBR}$. Then, we chose the one that results in the lowest threshold ($\alpha_{\rm th}$ or $N_{\rm th}$) as the lasing mode and calculated its wavelength and power. The dependence of the wavelength and optical power on i_d is implicitly expressed in (1) and (2). Fig. 21 shows a typical example of the tuning characteristic of the DBR laser calculated from the above modeling. Compared with Fig. 2(a), one can see a good agreement between the calculation result and the measurement. We matched Fig. 2(a) with the numerical model to the precision of a few percent.

APPENDIX B
MODELING OF OPTICAL WAVELENGTH FILTER

The optical filter used in this experiment has a Fabry–Perot (FP) etalon structure and its transmission function can be written as [28]

$$\frac{I_t}{I_i} = \frac{(1-R)^2}{(1-R)^2 + 4R\sin^2(\delta/2)} \tag{B1}$$

with

$$\delta = \frac{4\pi n l \cos\theta}{\lambda}. \tag{B2}$$

Here, n and l are, respectively, the index and thickness of etalon, θ is the internal angle of incidence, and R is the intensity reflectivity. Using the free spectral range (FSR) of the FP etalon $\Delta\nu = c/2nl\cos\theta$ and the resolution of the etalon $\nu_w = \Delta\nu/F_s$, one easily arrives at

$$\frac{I_t}{I_i} = \frac{A}{1 + \frac{4}{\pi^2}F_s^2 \sin^2\left[\frac{\pi(\lambda-\lambda_c)}{F_s\lambda_w}\right]} \tag{B3}$$

where $F_s \equiv \pi\sqrt{R}/(1-R)$ is the finesse of the etalon, A is the amplitude related with the transmission loss of the filter, and λ_c and $\lambda_w(=(\lambda/v)v_w)$ are the center wavelength and the wavelength bandwidth of the filter, respectively. We fitted the measured filter transmission characteristics shown in Fig. 2(b) with (B3) and found they agree with each other strikingly well. In fact, the standard error between the measurement of the filter used in this experiment and the calculation result based on the numerical model is as low as 0.6%.

ACKNOWLEDGMENT

The authors are grateful to B. Komiyama for support, and H. Fujino and K. Inagaki for valuable experimental help.

REFERENCES

[1] H. Fujisaka and T. Yamada, "Stability theory of synchronized motion in coupled-oscillator systems," *Prog. Theor. Phys.*, vol. 69, no. 1, pp. 32–47, 1983.
[2] L. M. Pecora and T. L. Carroll, "Synchronization in chaotic systems," *Phys. Rev. Lett.*, vol. 64, no. 8, pp. 821–824, 1990.
[3] K. M. Cuomo and A. V. Oppenheim, "Circuit implementation of synchronized chaos with applications to communications," *Phys. Rev. Lett.*, vol. 71, no. 1, pp. 65–68, 1993.
[4] C. M. Gray, P. König, A. K. Engel, and W. Singer, "Oscillatory responses in cat visual cortex exhibit inter-columnar synchronization which reflects global stimulus properties," *Nature*, vol. 338, pp. 334–337, 1989.
[5] A. M. Sillito, H. E. Jones, G. L. Gerstein, and D. C. West, "Feature-linked synchronization of thalamic relay cell firing induced by feedback from the visual cortex," *Nature*, vol. 369, pp. 479–482, 1994.
[6] P. Colet and R. Roy, "Digital communication with synchronized chaotic lasers," *Opt. Lett.*, vol. 19, no. 24, pp. 2056–2058, 1994.
[7] C. R. Mirasso, P. Colet, and P. Garcia-Fernandez, "Synchronization of chaotic semiconductor lasers: Application to encoded communications," *IEEE Photon. Technol. Lett.*, vol. 8, pp. 299–301, Feb. 1996.
[8] V. Annovazzi-Lodi, S. Donati, and A. Sciré, "Synchronization of chaotic lasers by optical feedback for cryptographic applications," *IEEE J. Quantum Electron.*, vol. 33, pp. 1449–1454, Sept. 1997.
[9] G. D. Van Wiggeren and R. Roy, "Communication with chaotic lasers," *Science*, vol. 279, pp. 1198–1200, 1998.
[10] J. P. Goedgebuer, L. Larger, and H. Porte, "Optical cryptosystem based on synchronization of hyperchaos generated by a delayed feedback tunable laser diode," *Phys. Rev. Lett.*, vol. 80, no. 10, pp. 2249–2252, 1998.
[11] S. Sivaprakasam and K. Shore, "Demonstration of optical synchronization of chaotic external-cavity laser diodes," *Opt. Lett.*, vol. 24, no. 7, pp. 466–468, 1999.
[12] Y. Takiguchi, H. Fujino, and J. Ohtsubo, "Experimental synchronization of chaotic oscillations in externally injected semiconductor lasers in low-frequency fluctuation regime," *Opt. Lett.*, vol. 24, no. 22, pp. 1570–1572, 1999.
[13] H. F. Chen and J. M. Liu, "Open-loop chaotic synchronization of injection-locked semiconductor lasers with gigahertz range modulation," *IEEE J. Quantum Electron.*, vol. 36, pp. 27–34, Jan. 2000.
[14] I. Fischer, Y. Liu, and P. Davis, Synchronization of chaotic semiconductor laser dynamics on sub-ns timescales and its potential for chaos communication, in *Phys. Rev. A*, vol. 62, no. 1, p. 011801-1-4, 2000.
[15] K. Ikeda and K. Matsumoto, "High-dimensional chaotic behavior in systems with time-delayed feedback," *Physica D*, vol. 29, pp. 223–235, 1987.
[16] H. D. I. Abarbanel and M. B. Kennel, "Synchronizing high-dimensional chaotic optical ring dynamics," *Phys. Rev. Lett.*, vol. 80, no. 14, pp. 3153–3156, 1998.
[17] A. R. Volkovskii and N. F. Rulkov, "Synchronous chaotic response of a nonlinear oscillator system as a principle for the detection of the information component of chaos," *Tech. Phys. Lett.*, vol. 19, no. 2, pp. 97–99, 1993.
[18] C. Ling and S. Sun, "Chaotic frequency hopping sequences," *IEEE Trans. Commun.*, vol. 46, pp. 1433–1437, 1998.
[19] J. K. White and J. V. Moloney, "Synchronization and communication with chaotic semiconductor lasers," in *Proc. NOLTA'97*, 1997, pp. 129–132.

[20] Y. Liu and J. Ohtsubo, "Chaos in an active interferometer," *J. Opt. Soc. Amer. B*, vol. 9, no. 2, pp. 261–265, 1992.
[21] L. Larger, J.-P. Goedgebure, and J.-M. Merolla, "Chaotic oscillator in wavelength: A new setup for investigating differential difference equations describing nonlinear dynamics," *IEEE J. Quantum Electron.*, vol. 34, pp. 594–601, Apr. 1998.
[22] Y. Liu and P. Davis, "Synchronization of chaotic mode hopping," *Opt. Lett.*, vol. 25, no. 4, 2000.
[23] A. Tsigopoulos, T. Sphicopoulos, I. Organos, and S. Pantelis, "Wavelength tuning analysis and spectral characteristics of three-section DBR lasers," *IEEE J. Quantum Electron.*, vol. 28, pp. 415–426, Feb. 1992.
[24] K. Kobayashi and I. Mito, "Single frequency and tunable laser diodes," *J. Lightwave Technol.*, vol. 6, pp. 1623–1633, Nov. 1988.
[25] Y. Kotaki and H. Ishikawa, "Spectral characteristics of a three-section wavelength-tunable DBR laser," *IEEE. J. Quantum Electron.*, vol. 25, pp. 1340–1345, June 1989.
[26] R. Hegger, H. Kantz, and T. Schreiber, "Practical implementation of nonlinear time series methods: The TISEAN packge," *Chaos*, vol. 9, no. 2, pp. 413–435, 1999.
[27] G. P. Agrawal and N. K. Dutta, *Semiconductor Lasers*, 2nd ed. New York: Van Nostrand Reinhold, 1993, pp. 32–50.
[28] A. Yariv, *Optical Electronics*, 3rd ed. New York: Holt, Rinehart and Winston, 1985, pp. 88–95.

Yun Liu, photograph and biography not available at the time of publication.

Peter Davis, photograph and biography not available at the time of publication.

Tahito Aida, photograph and biography not available at the time of publication.